13th International Symposium on Turbulence and Shear Flow Phenomena (TSFP13)
Montreal, Canada, June 25–28, 2024

AN EFFICIENT ALGORITHM FOR RESOLVENT AND HARMONIC RESOLVENT ANALYSES

Ali Farghadan
Department of Mechanical Engineering
University of Michigan
1231 Beal Ave, Ann Arbor, MI, 48109, USA
aliii@umich.edu

Aaron Towne
Department of Mechanical Engineering
University of Michigan
1231 Beal Ave, Ann Arbor, MI, 48109, USA
towne@umich.edu

ABSTRACT

We present a recent algorithm, known as RSVD-Δt, for computing resolvent and harmonic resolvent modes for large systems. Originally developed for stationary steady-state flows where resolvent analysis is applicable, we have extended this algorithm to encompass fluid flows exhibiting periodic motions at specific frequencies, necessitating harmonic resolvent analysis. The success of RSVD-Δt lies in its ability to eliminate the bottleneck associated with solving potentially large linear systems in frequency space and replace it with an efficient time-stepping surrogate whose cost scales linearly with the dimension of the problem. In particular, we emphasize the effectiveness of time-stepping for periodic flows, where the harmonic resolvent operator consolidates all frequencies of interest into a single matrix, unlike resolvent analysis, where a separate resolvent operator is constructed for each frequency. To illustrate the capabilities of RSVD-Δt, we compute resolvent modes for a three-dimensional jet and harmonic-resolvent modes for the flow around an airfoil.

INTRODUCTION

Modal analysis techniques, including spectral proper orthogonal decomposition (SPOD), dynamic mode decomposition (DMD), and resolvent analysis, have received a lot of attention in recent years (Taira *et al.*, 2017; Towne *et al.*, 2018). Among these techniques, resolvent analysis has emerged as a widely explored operator-theoretic method. It serves as a valuable tool for gaining insights into the dynamics of fluid flows. Nonetheless, computational challenges have largely prohibited its application to geometrically complex flows, especially those with three inhomogeneous dimensions.

Harmonic resolvent analysis is an extension of resolvent analysis that investigates flows characterized by a time-varying, periodic base flow, such as vortex shedding behind a cylinder (Padovan *et al.*, 2020). The frequency content of the base flow determines the number of triadic interactions between the forcing, base flow, and response. The singular value decomposition (SVD) of the harmonic resolvent operator is employed to determine the optimal forcing and identify the most amplified response. Standard resolvent analysis is recovered as a special case when the base flow becomes time-independent. However, the computational requirements for computing the leading harmonic-resolvent modes can be even more demanding than the resolvent case due to the higher dimensionality of the linearized operator caused by the aforementioned frequency coupling.

RESOLVENT ANALYSIS

The linearized Navier-Stokes (LNS) equations for statistically steady flows can be written as

$$\frac{\partial \boldsymbol{q}'}{\partial t} = \boldsymbol{A}(\bar{\boldsymbol{q}})\boldsymbol{q}' + \boldsymbol{f}'(\bar{\boldsymbol{q}},\boldsymbol{q}'), \tag{1}$$

where the state $\boldsymbol{q} \in \mathbb{C}^N$ is decomposed into the temporal average of the flow $\bar{\boldsymbol{q}}$, and the time-varying fluctuations $\boldsymbol{q}'$. Here, $\boldsymbol{f}'$ is the forcing, including the nonlinearities and external forces, $\boldsymbol{A} \in \mathbb{C}^{N\times N}$ is the LNS operator, and N is the state dimension of the discretized system. The resolvent system

$$\hat{\boldsymbol{q}}(\omega) = \boldsymbol{R}(\omega)\hat{\boldsymbol{f}}(\omega) \tag{2}$$

is obtained by taking a Fourier transform of (1). The resolvent operator

$$\boldsymbol{R} = (i\omega\boldsymbol{I} - \boldsymbol{A})^{-1} \in \mathbb{C}^{N\times N} \tag{3}$$

maps the forcing to the response in Fourier space (McKeon & Sharma, 2010). Here, ω denotes the frequency, $\boldsymbol{I}$ is the identity matrix, and $i = \sqrt{-1}$. The SVD

$$\boldsymbol{R} = \boldsymbol{U}\Sigma\boldsymbol{V}^* \tag{4}$$

identifies the optimal forcing $\boldsymbol{V}$ and response modes $\boldsymbol{U}$ along with their corresponding amplifications (gains) Σ.

HARMONIC RESOLVENT ANALYSIS

A similar Reynolds decomposition of Navier-Stokes equations can be applied to flows where the mean flow is periodic, yielding the time-dependent linear system,

$$\frac{\partial \boldsymbol{q}}{\partial t} = \boldsymbol{A}_p \boldsymbol{q} + \boldsymbol{f}, \tag{5}$$

where $\boldsymbol{A}_p(t) = \boldsymbol{A}_p(t+T) \in \mathbb{C}^{N\times N}$ is the periodic LNS operator, ω_f is the fundamental frequency, and $T = 2\pi/\omega_f$ is the fundamental cycle length. Taking the Fourier transform of (5), we obtain

$$\boldsymbol{T}\hat{\boldsymbol{q}} = \hat{\boldsymbol{f}}, \tag{6}$$

where $\boldsymbol{T}$ is an infinite dimensional block matrix written as

$$\boldsymbol{T} = \begin{bmatrix} \ddots & \vdots & \vdots & \vdots & \vdots & ⋰ \\ \dots & \boldsymbol{R}^{-1}_{-\omega_f} & \hat{\boldsymbol{A}}_{-\omega_f} & \hat{\boldsymbol{A}}_{-2\omega_f} & \hat{\boldsymbol{A}}_{-3\omega_f} & \dots \\ \dots & \hat{\boldsymbol{A}}_{\omega_f} & \boldsymbol{R}^{-1}_{0} & \hat{\boldsymbol{A}}_{-\omega_f} & \hat{\boldsymbol{A}}_{-2\omega_f} & \dots \\ \dots & \hat{\boldsymbol{A}}_{2\omega_f} & \hat{\boldsymbol{A}}_{\omega_f} & \boldsymbol{R}^{-1}_{\omega_f} & \hat{\boldsymbol{A}}_{-\omega_f} & \dots \\ \dots & \hat{\boldsymbol{A}}_{3\omega_f} & \hat{\boldsymbol{A}}_{2\omega_f} & \hat{\boldsymbol{A}}_{\omega_f} & \boldsymbol{R}^{-1}_{2\omega_f} & \dots \\ ⋰ & \vdots & \vdots & \vdots & \vdots & \ddots \end{bmatrix}, \tag{7}$$

where the diagonal entries are in fact the inverse of resolvent operators at various frequencies.

The harmonic resolvent operator is $\boldsymbol{H} = \boldsymbol{T}^{-1}$. The SVD

$$\boldsymbol{H} = \boldsymbol{U}_H \Sigma_H \boldsymbol{V}^*_H \tag{8}$$

provides the optimal forcing, response and degree of amplifications. In practice, one needs to truncate the frequencies to obtain $\boldsymbol{T}$, which forms a block matrix. The number of frequencies used to expand $\boldsymbol{A}_p$ in Fourier space determines the stencil length at each row (N_b), while the number of frequencies used to expand $\boldsymbol{q}$ determines the dimensions of the block matrices (N_ω). Hence, the overall size of $\boldsymbol{T}$ is $N_\omega N \times N_\omega N$.

THE RSVD-Δt ALGORITHM

RSVD-Δt utilizes time stepping to compute the action of the resolvent or harmonic resolvent operator on a vector (or matrix). In other words, given $\boldsymbol{b}$, we can compute $\boldsymbol{x} = \boldsymbol{R}\boldsymbol{b}$ or $\boldsymbol{x} = \boldsymbol{H}\boldsymbol{b}$ using time stepping. The original RSVD algorithm in the context of resolvent analysis (Moarref *et al.*, 2013; Ribeiro *et al.*, 2020) computes the LU decomposition of $\boldsymbol{R}$ and solves for $\boldsymbol{x}$ in Fourier space, referred to as "RSVD-LU" in this study. We, however, employ the steady-state response method, a technique utilized by both Martini *et al.* (2021) and Farghadan *et al.* (2023*b*) in the context of resolvent analysis, which has been generalized to harmonic resolvent analysis (Farghadan *et al.*, 2023*a*). Figure 1 illustrates the process of computing the action of the harmonic resolvent operator on a matrix. This approach leverages streaming calculations to minimize memory usage, resulting in only temporary storage of forcing inputs, LNS operators, and response snapshots in the time domain. The majority of memory allocation is dedicated to Fourier coefficients in the frequency space, and the streaming concept typically yields significant memory savings, often reducing memory usage by two or more orders of magnitude. A similar schematic can be drawn for computing the action of the resolvent operator on a matrix. In this scenario, the LNS operator remains constant and does not need to be stored in Fourier space.

Algorithm 1 RSVD-Δt for harmonic resolvent analysis

1: **Inputs:** $\boldsymbol{A}_p, k, q, \Omega_q, \Omega_{\tilde{q}}$, TSS, dt, T_t
2: $\hat{\Theta} \leftarrow \text{randn}(NN_\omega, k)$
3: $\hat{\boldsymbol{Y}} \leftarrow$ `DirectAction`$(\boldsymbol{A}_p, \hat{\Theta}, \text{TSS}, dt, T_t)$
4: **if** $q > 0$ **then**
5: $\quad\hat{\boldsymbol{Y}} \leftarrow \text{PI}(\boldsymbol{A}_p, \hat{\boldsymbol{Y}}, q, \text{TSS}, dt, T_t)$
6: **end if**
7: $\hat{\boldsymbol{Q}}_\Omega \leftarrow \text{qr}(\hat{\boldsymbol{Y}}_\Omega)$
8: $\hat{\boldsymbol{S}} \leftarrow$ `AdjointAction`$(\boldsymbol{A}^*_p, \hat{\boldsymbol{Q}}, \text{TSS}, dt, T_t)$
9: $(\tilde{\boldsymbol{U}}_H, \Sigma_H, \boldsymbol{V}_H) \leftarrow \text{svd}(\hat{\boldsymbol{S}}_H)$
10: $\boldsymbol{U}_H \leftarrow \hat{\boldsymbol{Q}}_\Omega \tilde{\boldsymbol{U}}_H$
11: **Outputs:** $\boldsymbol{U}_H, \Sigma_H, \boldsymbol{V}_H$

Algorithm 1: $k, q, \Omega_q, \Omega_{\tilde{q}}$ are common parameters with RSVD-LU. $(\cdot)_\Omega$ indicates all frequencies are merged into a single column, and TSS is an abbreviation for time-stepping schemes (*e.g.*, backward Euler). `DirectAction` and `AdjointAction` are functions that solve the direct and adjoint LNS equations, respectively, via time stepping with a predefined forcing.

The RSVD-Δt algorithm, as proposed by Farghadan *et al.* (2023*b*), has been extended to cover periodic flows with some modifications. This algorithm is built upon the RSVD algorithm, but the actions of the harmonic resolvent operator and its adjoint are replaced with the time-stepping surrogate. In contrast to the RSVD-LU algorithm, where constructing an expanded system of size $N_\omega N$ is necessary, RSVD-Δt leverages time integration directly on the LNS equations. This approach significantly reduces the size of the matrices involved, requiring only a system of size N. This fundamental difference in matrix size plays a pivotal role in the efficiency and scalability of RSVD-Δt for large-scale flows.

Algorithm 1 describes the RSVD-Δt algorithm for harmonic resolvent analysis, which contains as a special case standard resolvent analysis. Line 2 generates a random matrix $\hat{\Theta} \in \mathbb{C}^{NN_\omega \times k}$, which is used in line 3 to obtain the sketch of $\boldsymbol{H}$. This involves sampling the range of $\boldsymbol{H}$ via the `DirectAction` function, which computes the action of $\boldsymbol{H}$ on a given forcing using time-stepping before taking the Fourier transform. Optionally, power iteration (PI) can be performed as shown in lines 4 and 5, involving q successive applications of `DirectAction` and `AdjointAction` to improve the accuracy of the resolvent modes. In line 7, QR decomposition is applied to obtain the forcing to sample the image of $\boldsymbol{H}$ through `AdjointAction`. This function, similar to `DirectAction`, computes the action of $\boldsymbol{H}^*$ on a given forcing using time-stepping before taking a Fourier transform of the steady-state responses. An inexpensive SVD is performed in line 9, where the optimal forcing modes $\boldsymbol{V}_H \in \mathbb{C}^{NN_\omega \times k}$ and gains $\Sigma_H \in \mathbb{R}^{k\times k}$ of $\boldsymbol{H}$ are obtained. Line 10 recovers the optimal response modes $\boldsymbol{U}_H \in \mathbb{C}^{NN\omega \times k}$.

The steps of our algorithm in the context of resolvent analysis largely mirror those of Algorithm 1, except for two distinctions. In Algorithm 1, interactions between frequencies matter, requiring QR decomposition and SVD on all frequencies simultaneously. However, in resolvent analysis, each frequency is treated as a separate system, and QR and SVD are conducted individually for each frequency. Additionally, in Algorithm 1, the LNS operator $\boldsymbol{A}_j$ is generated at each time step (from $\hat{A}$ stored in memory as shown in figure 1), whereas

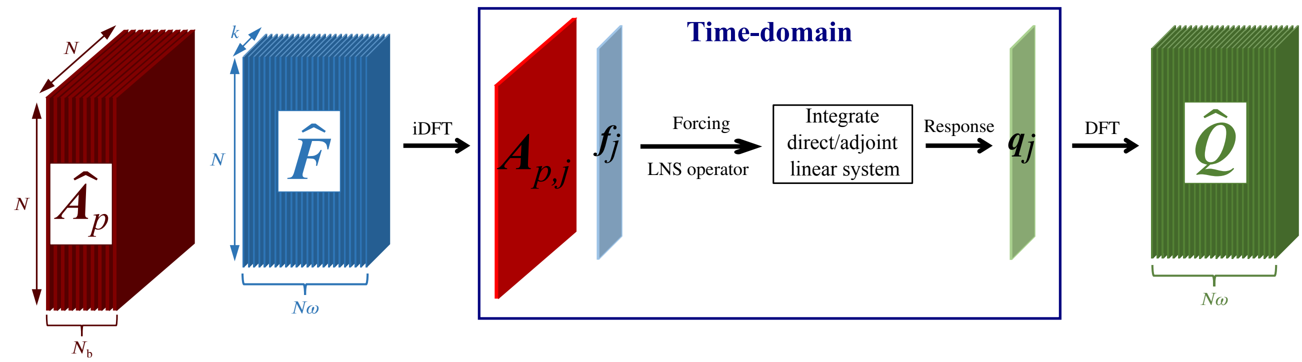

Figure 1. Schematic of the action of $\boldsymbol{H}$ with streaming discrete Fourier transform (DFT) and inverse DFT (iDFT) methods to transform between the Fourier and time domains. In resolvent analysis, $\boldsymbol{A}$ remains constant, and $\hat{\boldsymbol{A}}_{\boldsymbol{p}}$ vanishes.

in resolvent analysis, it remains constant throughout integration.

The main benefit of time-domain integration instead of solving a linear system in Fourier space is the scaling with dimension, as illustrated in figures 2 and 3. The scaling plots compare RSVD-LU (red lines) and RSVD-Δt (blue lines) in the context of resolvent analysis and harmonic resolvent analysis, respectively. In resolvent analysis, RSVD-LU scales as $O(N^{2.4})$ for CPU cost and $O(N^{1.5})$ for memory usage, while the CPU cost and memory usage of RSVD-Δt both increase linearly with dimension. In the harmonic resolvent analysis case study, the CPU scaling with the dimension of the RSVD-LU is theoretically comparable to resolvent analysis. However, it also scales with the number of frequencies involved in constructing the matrix $\boldsymbol{T}$. The computational cost scales with $O(N_\omega^{2.9})$, and the memory requirement scales with $O(N_\omega^{1.5})$, both determined by performing the LU decomposition of $\boldsymbol{T}$ with $N_b = 3$. This was achieved while maintaining a constant state dimension N and varying the number of blocks N_ω. With RSVD-Δt, the overall CPU cost remains unaffected by increasing N_ω. This implies that creating LNS operators on the fly and performing time-stepping are the dominant costs compared to the transformations between Fourier space and the time domain for forcing and response. Moreover, the primary memory usage of RSVD-Δt is to store the LNS operators, which is independent of N_ω, while the smaller portion required to store forcing and response matrices scales linearly with N_ω.

OPTIMIZING CPU AND MEMORY USAGE

Although streaming calculations have been shown to minimize memory consumption, and our algorithm computes resolvent modes for a range of frequencies simultaneously, additional strategies can be employed to further reduce both CPU time and memory usage.

In many cases, operators consist solely of real numbers, allowing us to exploit the symmetry of resolvent modes about zero. This property enables us to halve the memory usage for these matrices. Another crucial strategy involves reducing the duration of time stepping. This duration encompasses the time required to pass through transients and reach steady-state. Systems with slow decay rates require extended integration periods to eliminate undesired transient responses. By leveraging the underlying equations governing steady-state and transient responses, we can estimate and remove the transient part far more efficiently than waiting for natural decay. This approach can accelerate simulations by one or two orders of magnitude, depending on the desired accuracy and the system's original decay rate. Detailed descriptions of these strategies for resolvent and harmonic resolvent analyses are provided in Farghadan *et al.* (2023*b*) and Farghadan *et al.* (2023*a*), respectively.

TEST CASES

Our algorithm is showcased through two distinct configurations: one involving a jet for resolvent analysis, and the other featuring an airfoil for harmonic resolvent analysis.

ROUND TURBULENT JET

A round jet is employed to demonstrate the reduced computational cost and improved scalability of our algorithm. The mean flow is derived from a large eddy simulation (LES) utilizing the "Charles" compressible flow solver, with a Mach number of $M = \frac{U_j}{a} = 0.4$ and Reynolds number of $Re = \frac{U_j D_j}{\nu_j} = 0.45 \times 10^6$. Here, U_j represents the mean centerline velocity at the nozzle exit, a denotes the ambient speed of sound, ν_j signifies the kinematic viscosity at the nozzle exit, and D_j denotes the diameter of the nozzle. The computational domain extends over $x \in [0, 20]$ and $y \times z \in [-4, 4] \times [-4, 4]$, with grid resolutions of $400 \times 140 \times 140$, respectively. The range of Strouhal number, St, spans from 0 to 1, while an effective Reynolds number of 1000 is set to accommodate for unmodeled Reynolds stresses.

The resolvent operator is constructed around the three-dimensional mean flow. The LNS equations are expressed as $\boldsymbol{q}(\boldsymbol{x}, t) = [\xi, \boldsymbol{u}_x, \boldsymbol{u}_r, \boldsymbol{u}_\theta, \boldsymbol{p}]^T(\boldsymbol{x}, \boldsymbol{r}, \theta, t)$ comprising specific volume, the three velocity components, and pressure. The three-dimensional state in the frequency domain is

$$\boldsymbol{q}'(\boldsymbol{x}, \boldsymbol{y}, \boldsymbol{z}, t) = \sum_{\omega} \hat{\boldsymbol{q}}_\omega(\boldsymbol{x}, \boldsymbol{y}, \boldsymbol{z}) e^{i\omega t}, \tag{9}$$

and each mode is characterized by its frequency ω. To facilitate comparison, we also computed resolvent modes of an axisymmetric jet using identical mean flow variables across azimuthal wavenumbers of $m = 0, 1, 2,$ and 3. While solving an axisymmetric problem in 3D Cartesian coordinates may not be a practical approach, the rationale for this choice stems from the prohibitively high computational cost associated with computing the resolvent modes using RSVD-LU on a three-dimensional discretization of the jet. However, having insights into the modes at four azimuthal wavenumbers (Schmidt *et al.*, 2018) serves as a valuable benchmark for further assessment of our algorithm.

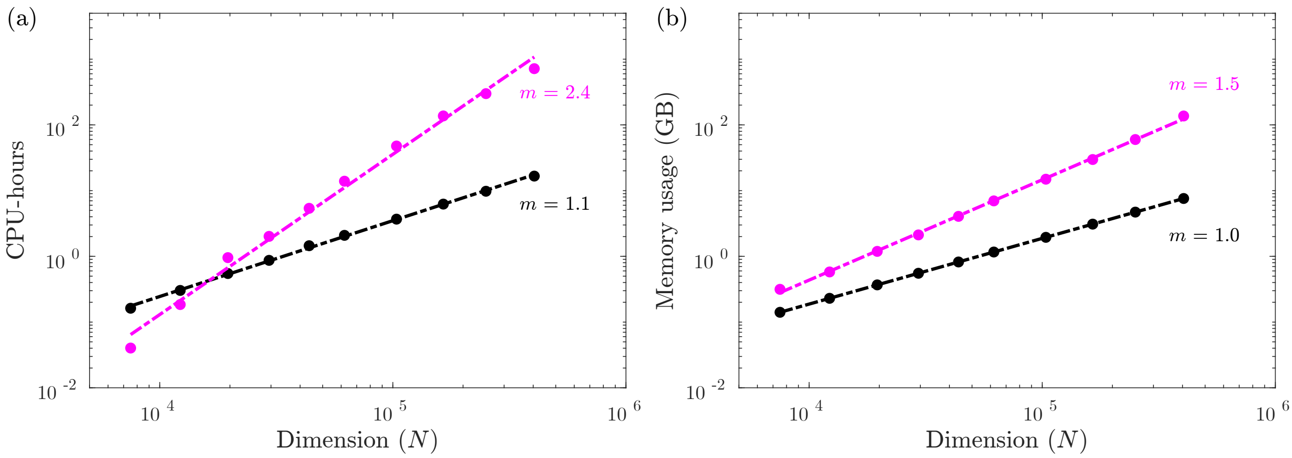

Figure 2. Computational cost of the resolvent analysis via RSVD-Δt as a function of the state dimension N for the three-dimensional jet: (a) CPU-hours and (b) memory usage for the RSVD-LU (pink) and RSVD-Δt (black) algorithms.

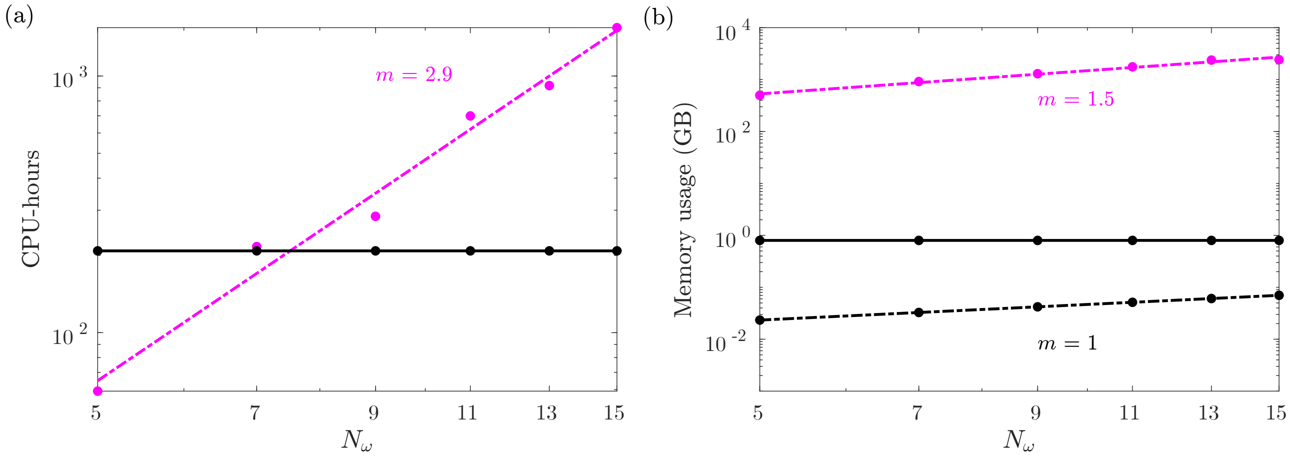

Figure 3. Computational cost of the harmonic resolvent analysis via RSVD-Δt as a function of N_ω for the airfoil test case: (a) The CPU-hour, and (b) memory usage scaling of RSVD-LU (pink) and RSVD-Δt (black) to compute the action of $\boldsymbol{H}$ onto a vector, *i.e.*, $k = 1$. The memory usage of RSVD-Δt is decomposed into memory required to store LNS operators (solid) and forcing and response matrices (dashed).

Resolvent modes for the three-dimensional round jet are computed using RSVD-Δt for the range of $St \in [0,1]$ with $\Delta St = 0.05$. The number of test vectors and power iterations are $k = 10$ and $q = 1$, respectively. The classical 4^{th} order Runge–Kutta (RK4) integrator with $dt = 0.00625$ is used for time stepping. The total integration length is set to $T = T_t + T_s = 3T_s$, based on the fact that the transient error drops below 1% for $St > 0$ when the transient duration of $T_t \approx 2T_s$ using our transient removal strategy. The resolvent modes of the axisymmetric jet are computed for the same St range using a standard Arnoldi-based method, serving as reference results.

We anticipate that the gains of the three-dimensional problem will encompass those of the axisymmetric problem due to the presence of azimuthal symmetry. Through a comparison of gains between two-dimensional and three-dimensional discretizations of the jet (figure not shown here), the RSVD-Δt reliably computes the three-dimensional resolvent modes and effectively captures the underlying physics of the problem. We present a comparative analysis of pressure response modes at various St numbers, corresponding to four distinct azimuthal wavenumbers, in figure 4. Each group showcases isocontours of the three-dimensional mode above and contours of the two-dimensional mode below. The cross-sectional views of each panel validate the expected azimuthal wavenumber classifications of each three-dimensional mode.

FLOW OVER AN AIRFOIL

We conduct our second test case on the flow dynamics around a NACA0012 airfoil, characterized by a Reynolds number of $Re = 200$ and an angle of attack of $\alpha = 20^\circ$. A direct numerical simulation via the “CharLES” compressible flow solver (Brès *et al.*, 2018) is performed to obtain the mean flow. The Mach number is set to 0.05 to replicate the conditions of an incompressible flow. The computational domain spans $x/L_c \times y/L_c \in [-49,50] \times [-50,50]$ with a leading edge at the origin $(x/L_c, y/L_c) = (0,0)$, and a chord length of $L_c = 1$. A constant time step of $\Delta t U_\infty / L_c = 6.88 \times 10^{-5}$ is utilized, corresponding to a CFL number of 0.91, where U_∞ represents the inflow streamwise velocity. Figure 5(a) depicts the power spectral density (PSD) computed from the transverse velocity at $(x/L_c, y/L_c) = (3.0, -0.43)$, where vortex shedding behind the trailing edge is evident. The shedding frequency is $St_f = 0.114$, where the Strouhal number is defined as $St = \frac{\omega L_c \sin(\alpha)}{2\pi U_\infty}$.

The domain of interest for harmonic resolvent analysis spans $x/L_c \times y/L_c \in [-4,12] \times [-2.5,2.5]$. Harmonic linearized operators are constructed at 100 time points within

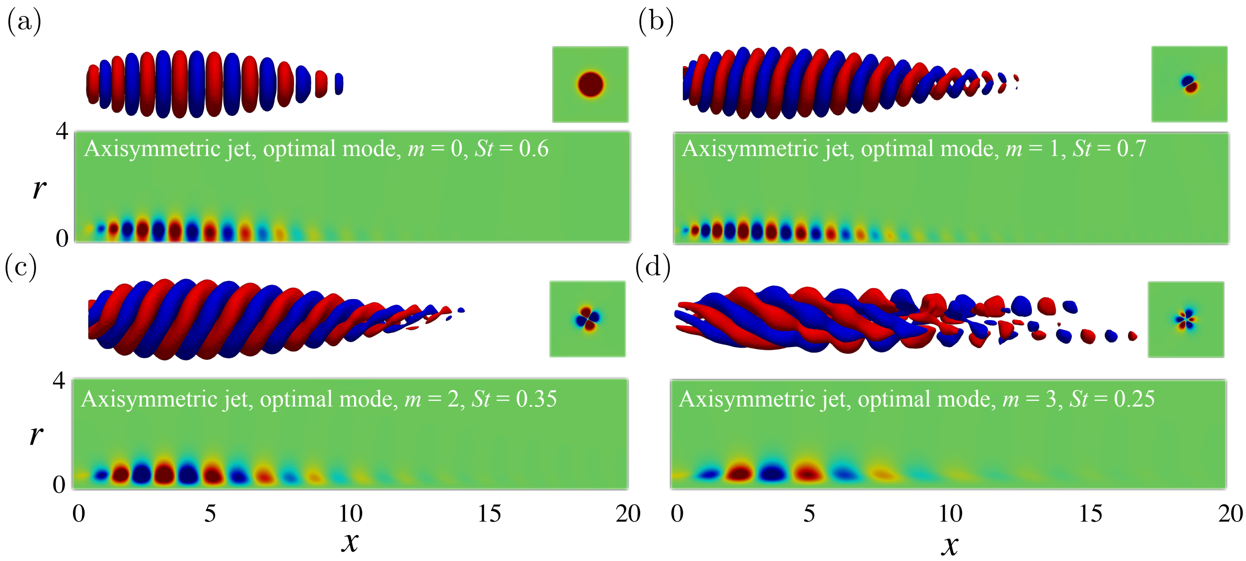

Figure 4. Four groups of axisymmetric and three-dimensional pressure modes are shown, including axisymmetric views, and three-dimensional iso-volume representations. Cross-sections at $x = 5$ confirm the azimuthal wavenumber of the three-dimensional results. Color bar ranges are adjusted for visualization.

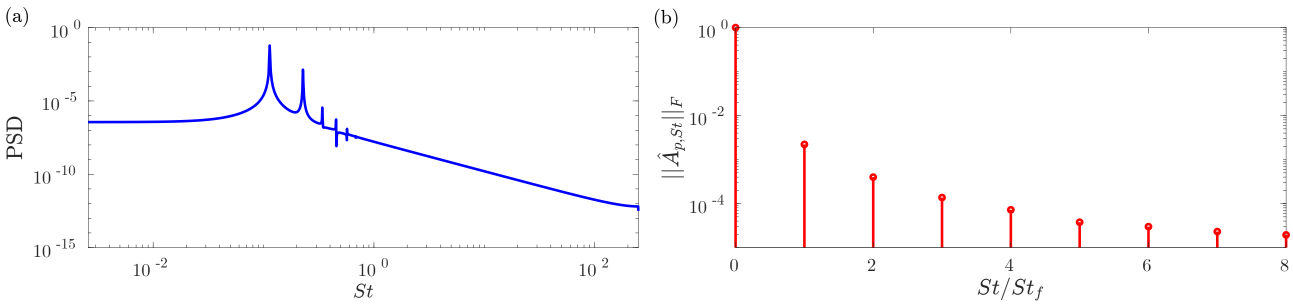

Figure 5. Airfoil test case: (a) the PSD spectrum based on transverse velocity at $(x/L_c, y/L_c) = (3.0, -0.43)$. (b) The normalized Frobenius norm of $\hat{\boldsymbol{A}}_{p,St}$ up to the eighth harmonic.

$T = 2\pi/St_f \approx 55$. Using a discrete Fourier transform (DFT), we generate 100 LNS operators $\hat{\boldsymbol{A}}j$ in Fourier space for harmonic resolvent analysis. Figure 5(b) presents the Frobenius norms of $\hat{\boldsymbol{A}}_{p,St}$, where we selected up to the 5^{th} harmonic in this study. To compute harmonic resolvent modes using RSVD-Δt, we employ the RK4 integration scheme with $dt = 0.0045$. The frequency range of the perturbation is set to $N_\omega = 15$, indicating that we assume the optimal perturbation and response does not contain frequencies beyond the 7^{th} harmonic. We set the total time-stepping length to $T = T_t + T_s = 30T_s$, indicating that employing our transient removal strategy for 29 periods is adequate to reduce the transient response error below 1%. Remarkably, without our transient removal strategy, the anticipated transient length would have exceeded 2000 periods, illustrating nearly two orders of magnitude in time stepping savings.

The number of test vectors is set to $k = 5$, with $q = 2$ power iterations effectively ensuring convergence of both gains and modes. Apart from the unwanted phase-shift mode (Padovan *et al.*, 2020), the optimal forcing and response modes are illustrated in figure 6. The intrinsic low-rank structure of this harmonic system results in a striking resemblance between the vortical structures observed in the first output mode and the vorticity patterns seen in the nonlinear simulation driven by sinusoidal perturbation (Padovan *et al.*, 2020). A key observation is that regardless of the type of perturbation, vortical structures dominate the flow dynamics. Furthermore, the forcing modes predominantly occur near the trailing edge, indicating the sensitive region of the airfoil for control and design purposes. Contrasting performance with performing resolvent analysis instead of harmonic resolvent analysis for flow around the airfoil reveals that the output only closely matches the base frequency and overlooks crucial physics at the mean flow and higher harmonics (Padovan *et al.*, 2020). This underscores the significance of harmonic resolvent analysis for flows characterized by dominant periodic motions. Finally, the results obtained from RSVD-Δt demonstrate close agreement with the existing data from RSVD-LU, as documented by Padovan *et al.* (2020), despite variations in the CFD solver, boundary conditions, domain setup, energy norm, and other factors. This underscores the reliability of RSVD-Δt in the context of harmonic resolvent analysis.

CONCLUSIONS

In conclusion, our newly developed algorithm for computing resolvent and harmonic resolvent modes presents a significant advancement by substantially reducing CPU and memory costs, thereby expanding the applicability of these tools to a broader range of problems. The computational complexity of RSVD-Δt is demonstrated to scale proportionally to the state dimension N in resolvent analysis. In harmonic resolvent analysis, where both forcing and LNS operators need

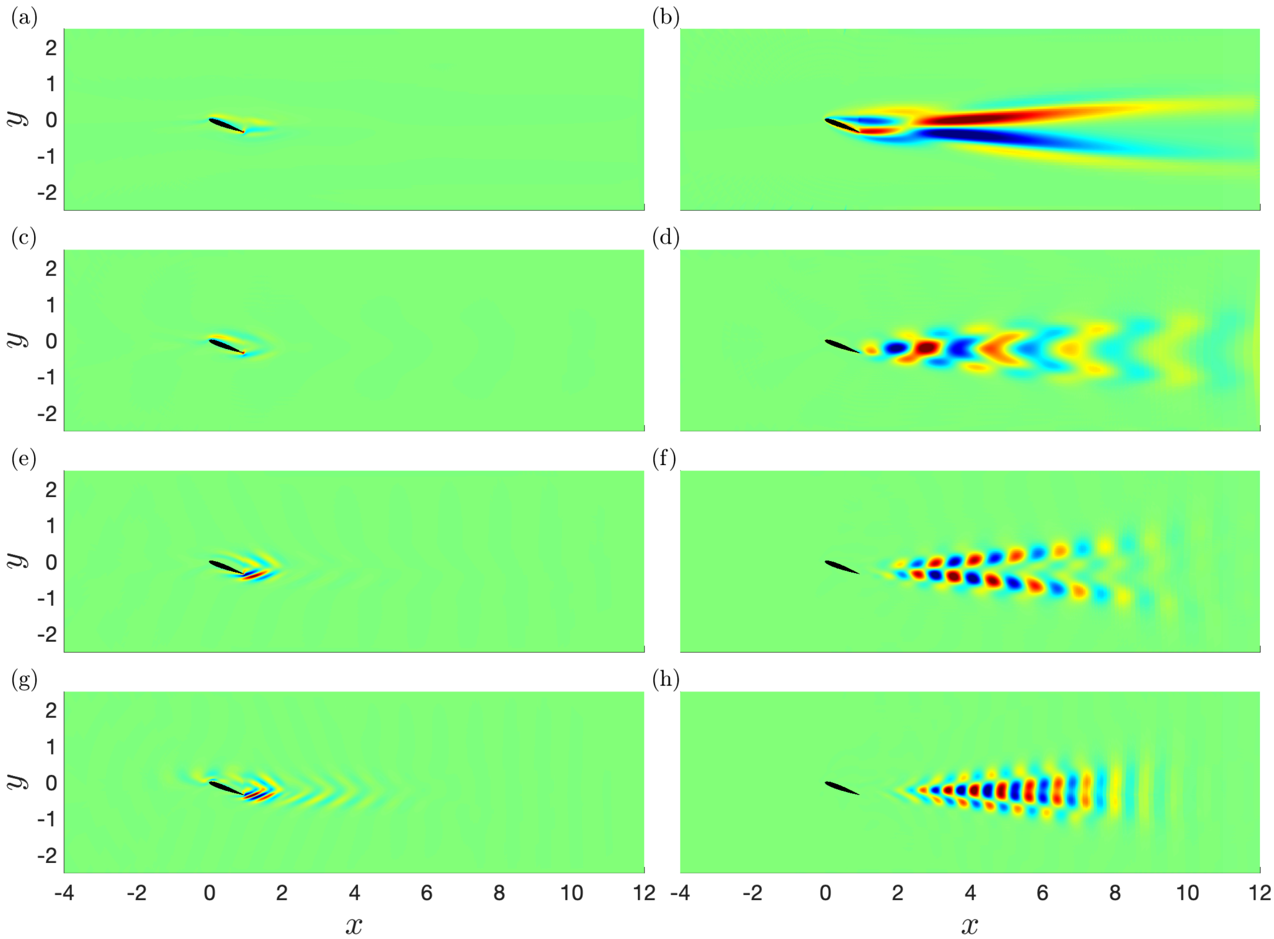

Figure 6. Airfoil test case: real part of the vorticity field computed from the optimal input (a, c, e, g) and output (b, d, f, h) modes at (a, b) $St = 0$, (c, d) $St = St_f$, (e, f) $St = 2St_f$, and (g, h) $St = 3St_f$, where St_f is the fundamental frequency. Color bar ranges are adjusted for visualization.

to be created at each iteration, RSVD-Δt still exhibits linear scalability, highlighting its effectiveness for periodic flow simulations. These findings underscore the potential of RSVD-Δt as a reliable and efficient tool for conducting resolvent and harmonic resolvent analyses across various domains.

REFERENCES

Brès, G. A., Jordan, P., Jaunet, V., Le Rallic, M., Cavalieri, A. V. G., Towne, A., Lele, S. K., Colonius, T. & Schmidt, O. T. 2018 Importance of the nozzle-exit boundary-layer state in subsonic turbulent jets. *Journal of Fluid Mechanics* **851**, 83–124.

Farghadan, A., Jung, J., Bhagwat, R. & Towne, A. 2023*a* Efficient harmonic resolvent analysis via time-stepping. *arXiv:2312.05766* .

Farghadan, A., Martini, E. & Towne, A. 2023*b* Scalable resolvent analysis for three-dimensional flows. *arXiv:2309.04617* .

Martini, E., Rodríguez, D., Towne, A. & Cavalieri, A. V. G. 2021 Efficient computation of global resolvent modes. *Journal of Fluid Mechanics* **919**, A3.

McKeon, B. J. & Sharma, A. S. 2010 A critical-layer framework for turbulent pipe flow. *Journal of Fluid Mechanics* **658**, 336–382.

Moarref, R., Sharma, A. S., Tropp, J. A. & McKeon, B. J. 2013 Model-based scaling of the streamwise energy density in high-Reynolds-number turbulent channels. *Journal of Fluid Mechanics* **734**, 275–316.

Padovan, A., Otto, S. E. & Rowley, C. W. 2020 Analysis of amplification mechanisms and cross-frequency interactions in nonlinear flows via the harmonic resolvent. *Journal of Fluid Mechanics* **900**, A14.

Ribeiro, J. H. M., Yeh, C. & Taira, K. 2020 Randomized resolvent analysis. *Physical Review Fluids* **5** (3), 033902.

Schmidt, O. T., Towne, A., Rigas, G., Colonius, T. & Brès, G. A. 2018 Spectral analysis of jet turbulence. *Journal of Fluid Mechanics* **855**, 953–982.

Taira, K., Brunton, S. L., Dawson, S. T. M., Rowley, C. W., Colonius, T., McKeon, B. J., Schmidt, O. T., Gordeyev, S., Theofilis, V. & Ukeiley, L. S. 2017 Modal analysis of fluid flows: An overview. *AIAA Journal* **55** (12), 4013–4041.

Towne, A., Schmidt, O. T. & Colonius, T. 2018 Spectral proper orthogonal decomposition and its relationship to dynamic mode decomposition and resolvent analysis. *Journal of Fluid Mechanics* **847**, 821–867.